

Partial tidal disruption of White Dwarfs in off-equatorial planes around intermediate mass spinning black holes

ARYABRAT MAHAPATRA ¹, ADARSH PANDEY ¹, DEBOJYOTI GARAIN ¹ AND TAPOBRATA SARKAR ¹

¹*Department of Physics, Indian Institute of Technology Kanpur, Kanpur 208016, India*

ABSTRACT

We present the results of a suite of numerical simulations to study partial tidal disruption events (TDEs) of white dwarfs (WDs) in off-equatorial planes in intermediate mass spinning (Kerr) black hole backgrounds. We carry out this analysis for both parabolic and eccentric WD orbits and also take into account possible initial WD spins. Our objective here is to quantify the differences in variables like the mass of the self-bound core, the peak fallback rate of debris and gravitational wave signature in off-equatorial orbits compared to equatorial ones. The analysis is carried out using a hybrid numerical scheme, one which involves integrating the exact Kerr geodesics while adopting a Newtonian formalism for the stellar fluid dynamics, justified by our choice of simulation parameters. We find that the physics of TDEs in off-equatorial orbits present several interesting and novel features due to black hole spin, which in some cases enhances when coupled with the rotation of the WD. However, numerical values of observable quantities in TDEs involving off-equatorial orbits cannot possibly distinguish between such orbits from equatorial ones. We further comment on the genericness of our results and argue that these should extend to a general TDE scenario involving a spinning BH.

1. INTRODUCTION

It is by now known that the physics of tidal disruption events (TDEs) of stellar objects in the background of spinning (Kerr) black holes (BHs) might be richer than the ones in the background of non-spinning ones (Wiggins and Lie 2000; Ivanov et al. 2003; Ishii et al. 2005; Ferrari et al. 2009; Kesden 2012b; Tejada et al. 2017; Banerjee et al. 2019; Gafton and Rosswog 2019; Jankovic and Gomboc 2023). In one of the first numerical studies on the subject, Haas et al. (2012) showed that the disruption process itself might depend strongly on the BH spin. However, in spite of the fact that rotating astrophysical BHs are possibly a more natural outcome of a gravitational collapse of a generic rotating star (Shibata 2003), literature on TDEs by Kerr BHs has been somewhat rarer. The topic was revived in a more recent paper by Gafton and Rosswog (2019), who considered deep (i.e., highly relativistic) TDEs of a solar-type star in the background of rotating supermassive black holes (SMBHs). In the context of Kerr BHs, recall that the solution is axially symmetric, thereby providing important departures in possible stellar trajectories when compared with the spherically symmetric Schwarzschild solution. In the latter case, due to spherical symmetry, any stellar orbit is effectively an equatorial one, a fact that is no longer valid for Kerr BHs. It is therefore important to ask how TDEs are affected by changing the inclination of stellar orbits in a Kerr BH background, i.e., when stars are in off-equatorial orbits about a Kerr BH.

This topic was first addressed by Kesden (2012b), who showed by semi-analytic methods that the peak accretion rate of tidally disrupted debris was achieved when the BH spin was anti-aligned with the stellar orbital angular momentum. A more recent analysis of TDEs in off-equatorial orbits, via loss cone theory, appear in Singh and Kesden (2024). While the work of Gafton and Rosswog (2019) considers a particular off-equatorial orbit in Kerr SMBH backgrounds, here we will address the issue of TDEs in generic off-equatorial planes for Kerr intermediate mass black holes (IMBHs). The purpose of the present analysis is two-fold. Firstly, recall that it is commonly believed that IMBHs (Volonteri 2012; Greene et al. 2020) maybe the “missing link” between the observationally more well established solar mass ($\sim 3 - 100M_{\odot}$) BHs and SMBHs ($\gtrsim 10^6M_{\odot}$). While evidence for the latter two is fairly abundant (Cherepashchuk

2016; Kormendy and Ho 2013), literature on the detection of IMBHs is relatively rarer, with only a handful being recently reported by (Kızıltan et al. 2017; Chilingarian et al. 2018; Takekawa et al. 2019; Abbott et al. 2020; Lin et al. 2020; Cao et al. 2023). Now since TDEs are widely considered as “smoking gun” signatures of BHs, it is important and interesting to understand TDEs in generic Kerr IMBH backgrounds, as this should reveal important information about IMBHs in general. Secondly, as we have already mentioned, studying TDEs in inclined, off-equatorial orbits for Kerr IMBHs is interesting in its own right. In particular, as already indicated by Singh and Kesden (2024), the physics of such events may be significantly different from TDEs in equatorial orbits. Our numerical analysis in this paper quantifies these issues, and we complement this further by considering stellar spin as well.

In this paper, we consider TDEs involving WDs in the background of Kerr IMBHs. From the mass-radius relation of Carbon-Oxygen WDs (Shapiro & Teukolsky 1983), it can be shown that these stars can be tidally disrupted either partially or fully by IMBHs : SMBHs will, in general, swallow the WD as a whole (Jonker et al. 2022). Since WDs also have a sufficiently accurate equation of state, these thus provide an attractive possibility of the study of Kerr IMBHs via TDEs. As we will discuss in detail below, here we study such TDEs by a suite of numerical simulations using smoothed particle hydrodynamics (SPH). We use a code that has been developed by us (Banerjee et al. 2023; Garain & Sarkar 2024a,b) and has been extensively compared and tested with the results available via the publicly available code PHANTOM. We use a hybrid formalism for our study, where the stellar particles follow geodesic trajectories in the Kerr IMBH background, while the hydrodynamics of the star are treated in a Newtonian manner. The stellar pericenter distance has been suitably chosen so that this last assumption for WDs is justified (Garain & Sarkar 2024b). In addition, we have considered spinning WDs in this work, although we do not consider magnetic fields usually associated with fast spinning WDs. Here we consider a spinning WD with a moderately fast rotation time period of 5 minutes (in contrast with the one reported by Kilic et al. (2021) that has a time period of ~ 70 seconds) so that this assumption can be justified.

Our results in this paper indicates that although the physics of TDEs indicate interesting subtleties in off-equatorial planes when compared to equatorial ones, it may not be possible to distinguish between such orbits by current observations via these events. As we argue below, this is a generic feature for TDEs of WDs with $M \lesssim 10^4 M_\odot$ IMBHs. To see this, we first record the formula of the tidal radius (Hills 1975)

$$r_t \approx R_\star \left(\frac{M}{M_\star} \right)^{1/3} \quad (1)$$

where M is the mass of the BH, and M_\star , R_\star being the mass and radius of the stellar object respectively. A star which approaches the BH and comes within r_t is tidally disrupted. In practise, this formula is approximate, and there are pre-factors due to stellar fluid dynamics, stellar spin etc. but this will not affect our qualitative discussion here.

Using the well known mass-radius relation for Carbon-Oxygen WDs, given in e.g. Equation 1 on page 39 in the article by Maguire et al. in Jonker et al. (2022), we obtain Figure 1, where we plot r_t/r_g where $r_g = GM/c^2$ is the gravitational radius of the BH as a function of the WD mass $M_{\text{WD}} = nM_\odot$ we have used the Chandrasekhar mass given by $1.435M_\odot$. In this figure, the pink horizontal line indicates the outer event horizon of a BH with dimensionless spin parameter $a^\star = 0.98$, below which WDs are captured as a whole rather than being tidally disrupted. From Figure 1, we see that for $M \gtrsim 5 \times 10^4 M_\odot$, most TDEs will be extremely relativistic, assuming an estimated cutoff of $r_t \leq 10r_g$ for these events (Stone et al. 2019), shown by the brown horizontal line if Figure 1. On the other hand, for lighter IMBHs with $M \lesssim 10^4 M_\odot$, using the fact that most known WDs have masses $\lesssim 0.8M_\odot$ (Kepler et al. 2004) indicated by the black vertical line in Figure 1, we see that a majority of TDEs of WDs with such IMBHs will be away from the relativistic regime. Our choice of parameters in this paper $M_{\text{WD}} = 0.5M_\odot$ corresponding to a radius $R_{\text{WD}} = 0.0141R_\odot$ and $M = 10^4 M_\odot$ is indicative of this regime and we can reasonably expect that our results would be generic for a majority of TDEs involving WDs and lighter IMBHs. We postpone further discussion on this to the final section of this paper, where we argue that these should extend to generic TDE events involving stars in off-equatorial Kerr orbits.

To contrast our discussion here with some known results in the literature, we recall that a useful measure of the strength of tidal interactions is the tidal tensor. This can be understood as the difference between the acceleration (force per unit rest mass) experienced by two neighboring particles of the stellar fluid and is conveniently defined by the spatial gradient of the acceleration. In the Newtonian case, the tidal tensor is $C_{ij} = -\frac{\partial^2 \Phi}{\partial x_i \partial x_j}$, with Φ being the Newtonian potential. In the relativistic regime, the tidal potential is more challenging to compute; for the Schwarzschild BH, it was obtained in Schwarzschild coordinates by Gafton et al. (2015). Popularly in the literature, one resorts to the Fermi normal coordinates (Manasse and Misner 1963) which gives a frame of reference locally flat along the geodesic

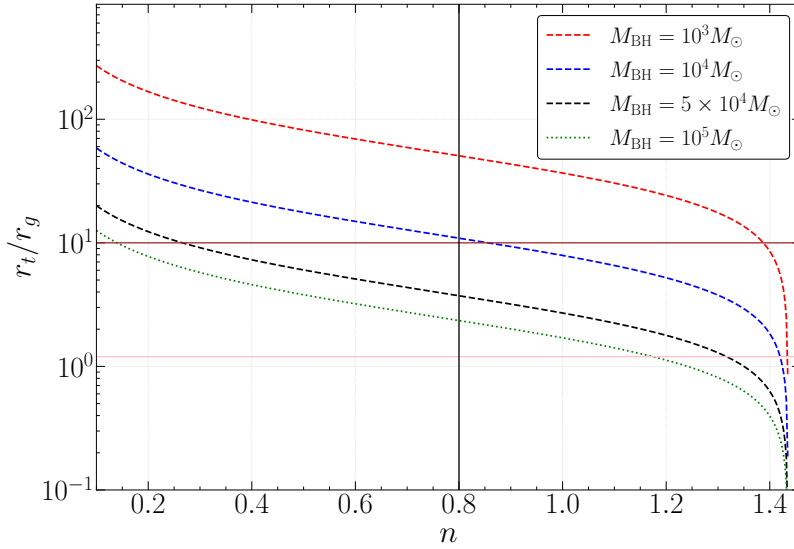


Figure 1. The tidal radius r_t plotted as a function of n where the WD mass $M_{\text{WD}} = n \times M_{\odot}$. The curved lines from top to bottom indicate BHs of 10^3 , 10^4 , 5×10^4 and 10^5 solar masses. The brown and pink horizontal lines indicate $r_t = 10$ and 1.2 respectively, while the vertical line indicates $n = 0.8$.

trajectory in which the center of mass of the star moves. In these coordinates, one can obtain a Newtonian potential as a perturbation series around the trajectory of the center of mass in powers of the distance from the same. For the Kerr BH, the tidal tensor in the Fermi normal frame expressed back in the standard Boyer-Lindquist coordinates in which the Kerr metric is written (see Equation 2) was computed by [Marck \(1983\)](#). As we will discuss in the final section of this paper, these results indicate broad similarity with ours. We emphasise however that Fermi normal coordinates apply to equilibrium stellar configurations and are less useful in a scenario where there is partial or full tidal disruption of the star. In such a situation where the dynamics is rather complicated, we require a numerical treatment to quantify the effect.

This paper is structured as follows: Section 2 discusses the methodology to simulate the tidal disruption in off-equatorial places around the Kerr BH using the SPH algorithm and the simulation parameters used in this work. Following this, in Section 3, we discuss the results obtained using our SPH code. Specifically, we study the impact of the off-equatorial planes and BH spin parameters on quantities such as mass disruption from the initial stellar object in case of partial disruption, fallback rates of the debris that is bound after the disruption, and gravitational wave (GW) amplitudes. Additionally, we extend our analysis by introducing a non-zero stellar spin to study the changes in observables. Finally, Section 4 concludes this paper with discussions and a summary of the results obtained.

2. METHODOLOGY

In this section, we discuss the methodology to simulate the tidal disruption of a stellar object in the off-equatorial planes around a Kerr BH. We employ the SPH algorithm to simulate the encounter between a BH and a stellar object, following the numerical algorithm developed by [Banerjee et al. \(2023\)](#), [Garain et al. \(2023\)](#), [Garain & Sarkar \(2024a\)](#), [Garain & Sarkar \(2024b\)](#). SPH is a Lagrangian-based method that conserves energy, linear momentum, and angular momentum. In SPH the fluid star is discretized into a collection of particles known as SPH particles, each possessing properties such as density, pressure, internal energy, velocity, etc. The properties and accelerations are smoothed using the M6 kernel function. To efficiently compute fluid properties and accelerations, we utilize the binary tree algorithm, as outlined in [Gafton & Rosswog \(2011\)](#). The tree-accuracy parameter (θ_{MAC}) is set to 0.5, which controls whether a distant node can be treated as a multipole source of gravity or further resolved into its descendants, for a given node. We use the standard SPH artificial viscosity term with the parameters $\alpha^{\text{AV}} = 1.0$ and $\beta^{\text{AV}} = 2.0$, and apply the Balsara switch to reduce viscosity in the shear flow following [Balsara \(1995\)](#). The SPH fluid equations are integrated using the Leapfrog integrator: a time-reversible and symplectic integration scheme given in [Springel \(2005\)](#) and [Hairer et al. \(2003\)](#). The global time-stepping is used for the evolution of the system, which ensures the minimization of

numerical errors as compared to individual time-stepping.

To simulate the tidal disruption of a stellar object around a Kerr BH on an inclined plane, we extend the code used by Garain & Sarkar (2024b). In Garain & Sarkar (2024b), the authors simulate tidal interactions in an equatorial plane to study the effects of BH spin and stellar spin on the observables related to the TDE. We extended the previous analysis by introducing the tidal interaction on an off-equatorial plane to study the change in observables from the equatorial plane tidal interactions. To do this, we need to fix the initial conditions, i.e., the initial coordinate: r_0, θ_0, ϕ_0 and the initial velocity: $\dot{r}_0, \dot{\theta}_0, \dot{\phi}_0$ of the center of mass of the stellar object. For example, we set: $r_0 = 5r_t$ from the BH positioned at the origin, $\theta_0 = \theta_a$ and $\phi_0 = 0$, where r_t is the tidal radius, and θ_a is the angle between the inclined plane and the BH spin direction. Now, to obtain the initial velocities, we need to specify the CM trajectory of the stellar object, which requires the specific energy \mathcal{E} , the specific angular momentum l_z (along the BH spin direction), and the Carter constant \mathcal{Q} (Carter 1968). In general, for a given type of orbit, it is also necessary to specify values of the turning points r_a, r_p , and θ_a , where r_a and r_p are the apocentre and pericentre of the orbit, respectively. The pericentre r_p of the orbit is determined using the tidal radius r_t and impact parameter β by the relation $r_p = r_t/\beta$, where the tidal radius is given by Equation 1. Once we obtain r_p , the apocentre r_a is obtained using r_p and eccentricity e of the orbit, via $r_a = r_p(1+e)/(1-e)$. However, specifying r_a and r_p alone is insufficient to determine the conserved quantities in the Kerr geometry for an inclined plane, as we discuss below.

The Kerr space-time geometry in Boyer-Lindquist (BL) coordinates (t, r, θ, ϕ) is expressed by the following metric:

$$ds^2 = - \left(1 - \frac{2GMr}{c^2\Sigma} \right) c^2 dt^2 - \frac{4GMra \sin^2 \theta}{c\Sigma} dt d\phi + \frac{\Sigma}{\Delta} dr^2 + \Sigma d\theta^2 + \left(r^2 + a^2 + \frac{2GMra^2 \sin^2 \theta}{c^2\Sigma} \right) \sin^2 \theta d\phi^2 \quad (2)$$

where $\Sigma = r^2 + a^2 \cos^2 \theta$ and $\Delta = r^2 - 2GMr/c^2 + a^2$. The Kerr parameter is defined as $a = J/Mc$. J and M denote the angular momentum and mass of the Kerr BH respectively, c is the speed of light and G is Newton's gravitational constant. The dimensionless Kerr parameter is given as $a^* = a/r_g$, where, as defined in the introduction, $r_g = GM/c^2$ is the gravitational radius of the BH. It can vary from -1 to +1, making the rotation of BH from retrograde to prograde, respectively.

To explore the tidal interactions in an off-equatorial plane along a general trajectory, the turning points of the trajectory is determined from $dr/d\tau = 0$. From Tejada et al. (2017), this relation is equivalent to setting $\mathcal{R}(r) = 0$, where $\mathcal{R}(r)$ is expressed using r_s and c as follows:

$$\mathcal{R}(r) = \epsilon r^4 + c^4 r_s r^3 - c^2 (l_z^2 + \mathcal{Q}) r^2 + l^2 r_s r - a^2 c^2 \mathcal{Q} \quad (3)$$

where $r_s = 2r_g$ is the Schwarzschild radius, l^2 is the square of total magnitude of specific angular momentum and $\epsilon \equiv \mathcal{E}^2 - c^4$. It is evident that the quantity $\mathcal{R}(r)$ is a fourth-order polynomial. Since $dr/d\tau$ vanishes at the turning points, we can rewrite Equation 3, corresponding to its four roots as:

$$\mathcal{R}(r) = \epsilon (r - r_a)(r - r_p)(r - r_c)(r - r_d), \quad (4)$$

where r_c and r_d are two additional roots. From Equations 3 and Equation 4, we can write the conserved quantities in terms of turning points as:

$$\epsilon = -\frac{c^4 r_s}{r_a + r_p + r_c + r_d}, \quad \mathcal{Q} = \frac{c^2 r_s r_a r_p r_c r_d}{a^2 (r_a + r_p + r_c + r_d)}, \quad l^2 = c^4 \frac{r_a r_p (r_c + r_d) + r_c r_d (r_a + r_p)}{r_a + r_p + r_c + r_d}, \quad (5)$$

$$l_z^2 = c^2 r_s \frac{a^2 (r_a r_p + r_c r_d + (r_a + r_p)(r_c + r_d) - a^2) - r_a r_p r_c r_d}{a^2 (r_a + r_p + r_c + r_d)}$$

Additionally, for the Kerr metric, the conserved quantities are related as $l^2 = c^2 \mathcal{Q} + (l_z c - a\mathcal{E})^2$ and from $d\theta/d\tau = 0$, we have $\mathcal{Q} = l_z^2 \cot^2 \theta_a - \epsilon a^2 \cos^2 \theta_a$ (Tejada et al. 2017). These two equations can be used along with the Equation 5, to obtain the following equations for the unknown turning points r_c and r_d :

$$r_a r_p r_c r_d - a^2 \cos^2 \theta_a (r_a r_p + r_c r_d + (r_a + r_p)(r_c + r_d) - a^2 \cos^2 \theta_a) = 0 \quad (6)$$

$$(a^2 (r_a + r_p + r_c + r_d - 2r_s) + r_c r_p (r_s - r_d) + r_d r_s (r_c + r_p) + r_a (r_c + r_d + r_p) r_s - r_a (r_c r_d + r_p (r_c + r_d)))^2 - 4r_s (r_a + r_p + r_c + r_d - r_s) (a^4 + r_a r_p r_c r_d a^2 (r_c r_d + r_p (r_c + r_d) + r_a (r_c + r_d + r_p))) = 0 \quad (7)$$

Since most of our analyses involve parabolic trajectories, the same mechanism can be applied to the parabolic limit $r_a \rightarrow \infty$ and $\mathcal{E} = c^2$, that is, $\epsilon = 0$. Under this limit, we arrive at a new set of equations, analogous to those found in Equation 6 and Equation 7, to determine r_c and r_d for the parabolic trajectory¹. Once we have r_p , r_a , r_c and r_d for any general trajectory, we can substitute it back into Equation 5 to get \mathcal{Q} , l^2 and l_z . Consequently, we can use these conserved quantities in the first integral of motion to obtain the initial velocities. Once we set the coordinates and velocities, these are then transformed into a Cartesian-like coordinate system and velocities, which are more suitable for our simulation. During tidal disruption, spherical symmetry breaks, therefore, Cartesian-like coordinates are more convenient to capture the dynamics during the time evolution accurately. Finally, with these initial conditions and the Kerr geodesics accelerations, we obtain the time evolution of the stellar object in the presence of a Kerr BH along an off-equatorial trajectory.

After specifying the geodesics, we proceed to configure the details of the stellar object, which is modeled as a WD in our simulations. We follow the methodology outlined in Garain & Sarkar (2024b) to obtain the relaxed WD configuration in SPH. Initially, we derive the theoretical density profile $\rho(r)$ of WD by solving the hydrostatic equilibrium and mass conservation equations (Chandrasekhar 1935; Shapiro & Teukolsky 1983), which are then incorporated into the SPH framework. In our simulations, SPH particles are initially arranged in a closed-packed sphere, which is subsequently stretched using the stretch mapping technique (Herant 1994) to match the theoretical density profile of the WD. This approach reduces computational costs compared to random particle placements. To minimize fluctuations in fluid properties introduced during stretch mapping, the WD evolves in isolation, without external forces. The final relaxed state is achieved when the ratio of total kinetic energy and total gravitational energy falls below a tolerance of 10^{-6} and the density profile converges to the theoretical density profile of WD.

To construct a uniformly rotating WD, following García-Senz et al. (2020), we impose rigid rotation on the previously relaxed non-rotating WD configuration. To reduce noise in velocity, and achieve equilibrium quickly, velocities are periodically reset to zero in the comoving reference frame, initially at shorter intervals and later at longer intervals. Once the angular velocity settles within 0.1% of the desired angular velocity, the system evolves freely without resetting the velocity to check whether the central density, the equatorial and polar radii, and the energies oscillate within 2.5% of their average values. Finally, relaxed rotating WD configurations are considered to form when all these properties remain within the specified tolerance for a sufficiently long duration. The maximum angular velocity of a star that can be sustained without breaking apart is determined by equating the self-gravitational force with the centrifugal force given by $\Omega_{\text{br}} = \sqrt{GM_*/R_*^3}$. Here, we will use the dimensionless quantity known as the breakup fraction, defined as $\lambda = \Omega_{\text{WD}}/\Omega_{\text{br}}$ where Ω_{WD} is the angular velocity of the spinning WD.

2.1. Simulation Parameters

In this work, we adopt a wide range of combinations of all parameters required to explore the tidal interaction between a highly spinning Kerr BH and a Carbon-Oxygen WD. We examine a stellar object orbiting a BH in two configurations: a parabolic orbit with eccentricity $e = 1$ and an elliptical orbit with $e = 0.9$, both with a pericenter distance $r_p \approx 25r_g$. In this paper, we consider the impact parameter $\beta = 0.7$ that corresponds to partial disruption scenarios of a WD due to an IMBH. It is still reasonable to consider the stellar hydrodynamics to be Newtonian for this choice of r_p , following the discussion of Stone et al. (2019). We consider a Kerr BH of mass $10^4 M_\odot$, falls within the IMBH regime and a $0.5 M_\odot$ of WD, whose radius is obtained as $0.0141 R_\odot$ from the corresponding Chandrasekhar mass-radius relation (Shapiro & Teukolsky 1983). We take the interacting WD to be both non-spinning and spinning with the maximum spin period around 300s corresponding to a break-up fraction $\lambda = 0.08$. This will significantly preserve the spherical shape of the WD. We have verified that in our case the aspect ratio, defined as the ratio of the equatorial to the polar radius of the WD is maintained around ≈ 1.001 . The relative difference in the tidal radius of spinning WDs from its non-spinning counterpart is less than 1% according to the effective tidal radius formula of Golightly et al. (2019a).

In our simulation, we always fix the Kerr IMBH spin along the z -direction. Now, we will have a plethora of options for configuring our simulations to take place on any inclined orbit around the Kerr IMBH, with an inclination angle ranging from $\theta_a = 0^\circ$ to $\theta_a = 180^\circ$, which fixes the orbital angular momentum (perpendicular to that orbital plane). Once we fix our orbit, it is necessary to set the spin angular momentum of the spinning WD. To draw significant

¹ For a parabolic trajectory, we proceed by setting $\mathcal{R}(r) = 0$, which corresponds to a third-order polynomial. This can be rewritten as $\mathcal{R}(r) = c^2 r_s (r - r_p)(r - r_c)(r - r_d)$.

observational consequences, we will only focus on the cases that result in maximum (or minimum) effects on physical variables. Here the spin angular momentum of spinning WD can be parallel or antiparallel with its orbital angular momentum.

We take into account that the Kerr parameter is $a^* = -0.98$ and $a^* = +0.98$ by altering the angle of inclination at $\theta_a = 1^\circ$ and at $\theta_a = 90^\circ$. The angle of inclination $\theta_a = 0^\circ$ leads to a divergence in the formalism, $\theta_a > 90^\circ$ is redundant by virtue of the symmetry, and the angles between $\theta_a = 1^\circ$ and $\theta_a = 90^\circ$ correspond to intermediate results of the effects of tidal disruption. In addition, we choose the break-up fraction values $\lambda = +0.08$, prograde motion (aligned with orbital rotation) and $\lambda = -0.08$ retrograde motion (aligned opposite to orbital rotation) because only these choices can pronounce the tidal disruption effects (Garain & Sarkar 2024b; Golightly et al. 2019a). For our partial disruption scenarios, we identify the self-bound core particles formed after the disruption using an energy-based iterative method following Guillochon & Ramirez-Ruiz (2013). The core formed after the partial disruption having high-density results in extremely small time steps, which slows down the system’s evolution. To efficiently evolve the system, once the core moves away from the BH and its properties are saturated, the core is replaced by a sink particle to speed up the simulation. The method for introducing the sink particle follows Garain et al. (2023); Price et al. (2018), and tests showed no impact on the fallback rate when adjusting the sink placement time. In our simulations, we replaced the core with a sink particle at approximately 0.24 hours.

We modeled relaxed WD using 5×10^5 SPH particles. Furthermore, we have checked the convergence of our results with 10^6 particles.

3. RESULTS

In this section, we explore the outcomes of the TDE of a WD following an off-equatorial trajectory around a Kerr BH. First, we focus on the mass loss from the WD due to partial disruption, and the distribution of debris in terms of specific energy. Following that, we discuss the impact of tidal interactions on key observables, including fallback rates, kick velocities, and GW emission during pericenter passage.

3.1. Mass Disruption

To begin, we explore the effects of orbital inclination on the resulting self-gravitating core and debris mass distribution in the absence of WD spin for a parabolic orbit. This is then compared to a more bound interaction, where the WD follows an eccentric orbit with the mentioned eccentricity of $e = 0.9$. Subsequently, we investigate how introducing an initial WD spin influences the core mass fraction, defined as the ratio of the core mass to the initial mass of the WD. due to the coupling between the WD spin, its orbital angular momentum and BH spin.

e	Relative difference in $M_{\text{core}}/M_{\text{wd}}$ b/w $\theta_a = 1^\circ$ & $\theta_a = 90^\circ$ planes		Relative difference in $M_{\text{core}}/M_{\text{wd}}$ b/w BH spins $a^* = +0.98$ & $a^* = -0.98$	
	$a^* = +0.98$	$a^* = -0.98$	$\theta_a = 1^\circ$	$\theta_a = 90^\circ$
	1.0	6.42 %	11.29 %	0.31 %
0.9	8.51 %	24.04 %	0.57 %	26.70 %

Table 1. Comparison of the relative difference in $M_{\text{core}}/M_{\text{wd}}$ between two inclined orbits for the specified values of a^* and θ_a , in parabolic and eccentric orbits, in the absence of WD spin.

In the absence of spin of the WD, we illustrate the resulting core mass fraction in Figure 2. Fixing the BH spin (at $a^* = \pm 0.98$) and considering inclined orbits at $\theta_a = 1^\circ$ and $\theta_a = 90^\circ$, we observe two distinct results in terms of the total mass disrupted from the initial WD. The disruption is found to be maximal in the $\theta_a = 1^\circ$ plane and minimal in the $\theta_a = 90^\circ$ plane for $a^* = 0.98$. We then repeat this analysis for a BH spin of $a^* = -0.98$. This time, the results are reversed: the disruption is minimal in the $\theta_a = 1^\circ$ plane and maximal in the $\theta_a = 90^\circ$ plane. The relative difference² of bound core mass fraction between the two inclined planes are given in Table 1. These results are collectively presented on the left panel of Figure 2, where the four mass disruption curves are plotted on a normalized mass and time scale. Examining the first row and comparing the first and second columns of Table 1 shows that a negative BH spin has the most significant effect on the tidal disruption of the WD. Additionally, we find that for the $\theta_a = 90^\circ$ plane, the

² The relative difference b/w equatorial and off-equatorial planes is computed by taking the equatorial plane, as the reference. Likewise, the relative difference b/w BH spins is computed by taking the $a^* = +0.98$ as the reference.

relative change in the core mass fraction by changing the BH spin parameter from $a^* = -0.98$ to $a^* = 0.98$ results in significant deviations. On the other hand, in the $\theta_a = 1^\circ$ plane, the curves for both positive and negative BH spins almost coincide, showing little to no distinction to the two spins of the BH. This distinctive feature of the inclination effect³ is preserved even when the WD follows an elliptical orbit, as shown in the right panel of Figure 2. However, we observe that the core mass fraction for the elliptical orbit is lower than that of the parabolic orbit when the BH spin parameter and inclination angle are fixed. This is more likely to happen as the WD passes in a more bound orbit, causing it to spend a longer duration in the region of strong tidal interaction. The relative difference in core mass fraction between different combinations of a^* and θ_a is presented in Table 1.

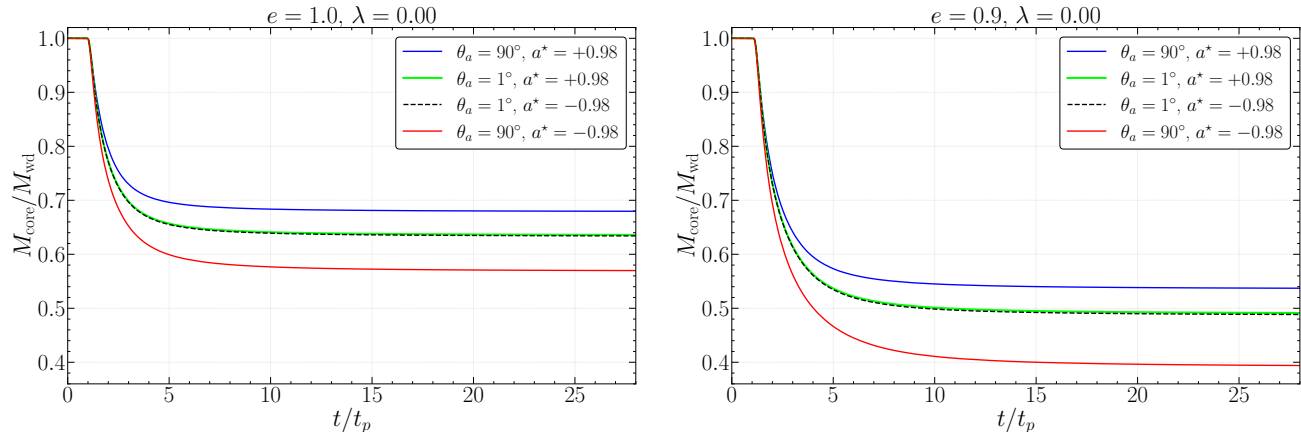


Figure 2. The core mass fraction, $M_{\text{core}}/M_{\text{wd}}$, is plotted against the normalized time t/t_p for the specified values of inclination angle, θ_a and BH spin, a^* . **Left Panel** shows the variation for a parabolic orbit, whereas **Right Panel** shows the variation for an eccentric orbit with $e = 0.9$.

Next, we analyze the differential mass distribution of the debris with specific energy for both the parabolic and elliptical orbits. Parabolic orbits lead to the formation of two distinct tidal tails along with the self-gravitating core (Gafton et al. 2015; Manukian et al. 2014), with one tail consisting of part of the debris which is bound to the BH with negative specific energy and the other consists of the part which is unbound from the BH with positive specific energy. This is also evident in our calculation of the differential mass distribution of the debris, which is obtained once the core mass saturates to form a self-bound object. In the left panel of Figure 3, we have computed the differential mass distribution, $dM/d\epsilon$, for the debris of both tidal tails of the WD in a parabolic orbit, using the post-disruption snapshot taken at $t \approx 0.22$ hr (i.e., no mass accreted at this time). The debris differential mass distribution is plotted against the specific energies, measured in units of the spread in specific energy of the debris, $\Delta\epsilon = GMR_{\text{wd}}/r_t^2$, for four different configurations of BH spins and inclined orbits. The effect of inclination in all these configurations follows a similar outcome, where the curves corresponding to the $\theta_a = 1^\circ$ planes overlap for both $a^* = \pm 0.98$. In contrast, the equatorial plane shows different results for $a^* = \pm 0.98$. In the elliptical orbit case, the differential mass distribution profiles are enhanced and feature higher peaks compared to the parabolic case, reflecting a greater extent of mass disruption, see the right panel of Figure 3. In this case, we have used the post-disruption snapshot taken at $t \approx 0.11$ hr, after the saturation of bound core mass and before the accretion of debris. However, we observe that this distribution primarily occurs for negative values of specific energy, as in our case, the tidal tails in elliptical orbits correspond mostly to bound debris. It can also be verified from Hayasaki et al. (2018), that the simulation parameters considered here in our work satisfy the condition $e_{\text{crit}}^- < e < 1$, where $e_{\text{crit}}^- = 1 - (2/\beta)q^{-1/3}$ with the mass ratio $q = M/M_*$. In our case, with $e_{\text{crit}}^- = 0.89$, the elliptical orbit ($e = 0.9$) is marginally eccentric. As a result, most of the debris remains bound to the BH, with only a small fraction becoming unbound. In general, tidal disruption phenomena occurring in off-equatorial trajectories are usually understood by examining the relative tidal strength in various inclined planes. Several studies, such as Mummery (2024); Kesden (2012a); Singh and Kesden (2024), have highlighted the implications of inclination effects in the context of TDEs. It has been shown that a star

³ We attribute this inclination effect to the fact that the outcome in the $\theta_a = 1^\circ$ plane is the same for both BH spins, $a^* = \pm 0.98$. Furthermore, this outcome lies between the distinct outcomes observed for $\theta_a = 90^\circ$, $a^* = +0.98$ and $\theta_a = 90^\circ$, $a^* = -0.98$.

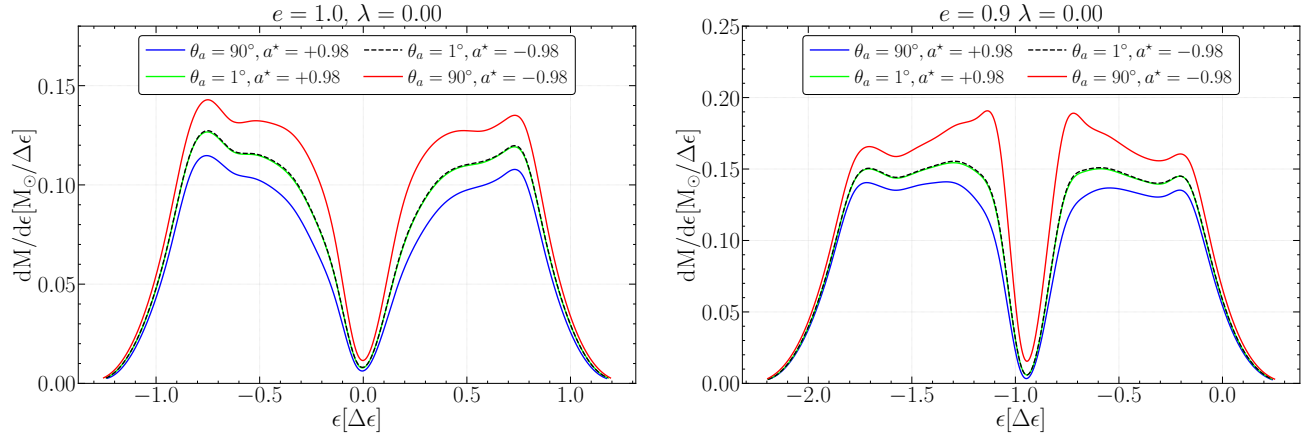


Figure 3. The differential mass distribution, $dM/d\epsilon$, is plotted against the normalized specific energy ϵ for the specified values of inclination angle, θ_a and BH spin, a^* . **Left Panel** shows the variation for a parabolic orbit, whereas **Right Panel** shows the variation for an eccentric orbit with $e = 0.9$

orbiting in the equatorial plane with negative BH spin ($a^* = -0.98$) experiences the highest tidal interaction, while the lowest occurs with positive BH spin ($a^* = +0.98$). Stars orbiting in other inclined planes experience intermediate tidal strengths relative to these extreme cases. These features have been explained by analyzing tidal accelerations using geodesic deviation equations. However, calculating the eigenvalues of the tidal tensor in the off-equatorial Kerr metric is extremely challenging in BL coordinates. Therefore, these studies have instead calculated tidal accelerations that depend on BH spin and inclination angle using Fermi Normal coordinates. In this work, we sidestep this issue by directly examining the test particle trajectories and analyzing how their accelerations vary with radial distance, offering an intuitive explanation for the inclination-dependent effects.

We consider the same initial conditions as chosen for our simulations for the test particle. In the top left panel of Figure 4, we show the projection of test particle geodesics on the y - z plane, corresponding to motion in the $\theta_a = 1^\circ$ plane around a Kerr BH with both spins. Regardless of the BH spin, the trajectories overlap and show little discernible difference due to the spin. The bottom left panel of Figure 4 illustrates test particle geodesics in the $\theta_a = 90^\circ$ plane, which is confined to the x - y plane. In this case, the trajectory for $a^* = -0.98$ brings the test particle into closer proximity after pericenter passage as compared to the $a^* = 0.98$ case, due to the larger apsidal precession. Finally, in the right panel of Figure 2, we present the variation of test particle acceleration as a function of radial distance. It is evident that in the $\theta_a = 1^\circ$ plane, the test particle experiences the same acceleration for both BH spins. Additionally, focusing on the region near the pericenter (around $r_p \approx 1.43r_t$), we observe that the test particle in the $\theta_a = 90^\circ$ plane, with $a^* = -0.98$, experiences the highest acceleration, while the particle with $a^* = +0.98$ experiences the least. The test particle in the $\theta_a = 1^\circ$ plane has an intermediate influence for both BH spins. Using this notion, at the pericenter, we can interpret that WD experiences similar tidal effects in the $\theta_a = 1^\circ$ plane for both BH spins. However, in the equatorial plane, it experiences the highest and lowest tidal effects for BH spins $a^* = -0.98$ and $a^* = +0.98$, respectively. Thus, in the $\theta_a = 1^\circ$ plane, we observe the same bound core mass fraction for both BH spin values, while in the equatorial plane, the bound core mass fraction varies depending on the BH spin. As a result, the $\theta_a = 1^\circ$ plane gives rise to the same amount of disrupted mass, consisting of bound and unbound debris, leading to identical debris differential mass distribution profiles for both BH spins. However, in the equatorial plane, the debris differential mass distribution profile is most enhanced for the negative BH spin due to the higher amount of debris, while the opposite occurs for the positive BH spin. When the spin is introduced to WD, the outcomes reflect similar trends as discussed earlier in [Garain & Sarkar \(2024b\)](#). Even in the $\theta_a = 1^\circ$ plane, the trends of mass disruption remain consistent. Significant changes are primarily observed in cases where the spin of WD is either aligned or anti-aligned with its orbital angular momentum. As expected, mass disruption is enhanced in the prograde motion of the WD ($\lambda = +0.08$) and suppressed in the retrograde motion of the WD ($\lambda = -0.08$). The changes in the $\theta_a = 1^\circ$ plane are observed solely due to the coupling effect between the WD spin and its orbital angular momentum, with little influence from the BH spin. However, in the equatorial plane, the coupling of the BH spin with the WD spin and the orbital angular momentum leads to distinct outcomes, as explained in [Garain & Sarkar \(2024b\)](#). We have verified that when the same WD spin is introduced (either $\lambda = 0.08$ or $\lambda = -0.08$), these changes occur while preserving the

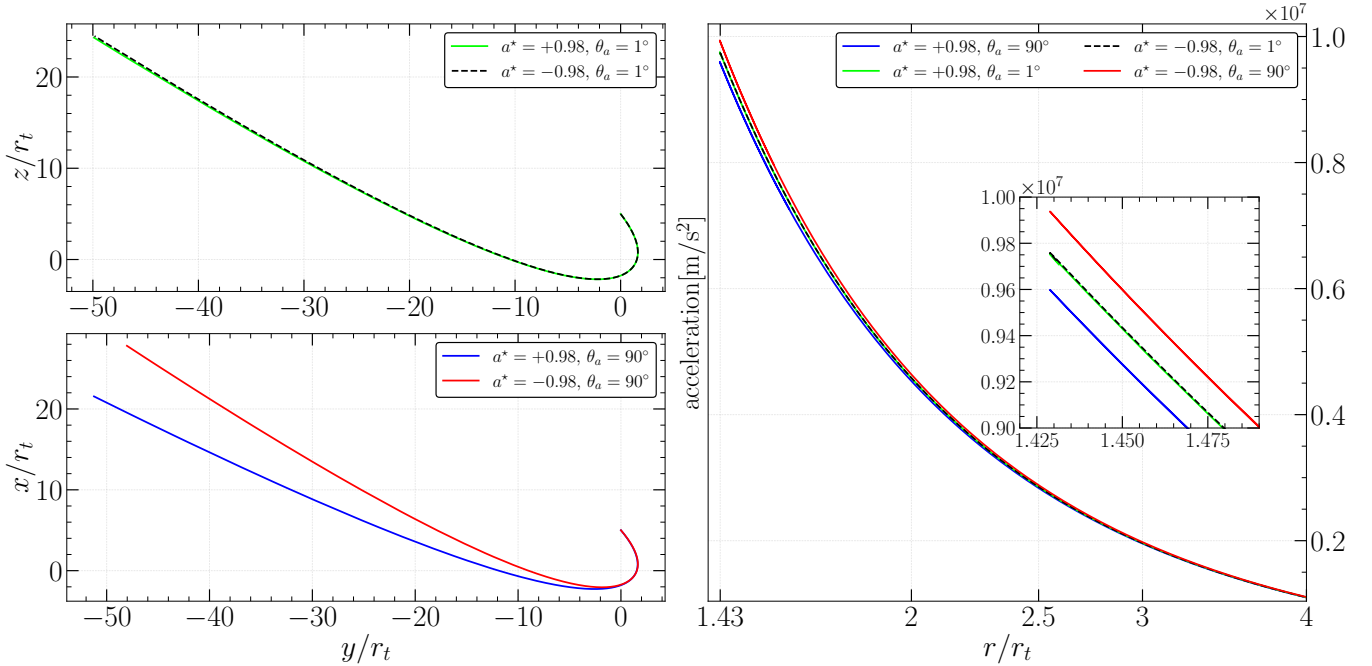


Figure 4. Geodesics and accelerations for a test particle orbiting in an off-equatorial parabolic orbit around a Kerr BH at the origin with spin $a^* = \pm 0.98$. The coordinates and distances are normalized with tidal radius, r_t of the BH. **Top Left Panel:** The y - z projection of the test particle's trajectory in the inclined plane $\theta_a = 1^\circ$. **Bottom Left Panel:** The trajectory of the test particle for $\theta_a = 90^\circ$, i.e., on the x - y plane (equatorial orbit). **Right Panel:** The variation of the magnitude of the acceleration with radial distance for all the specified cases.

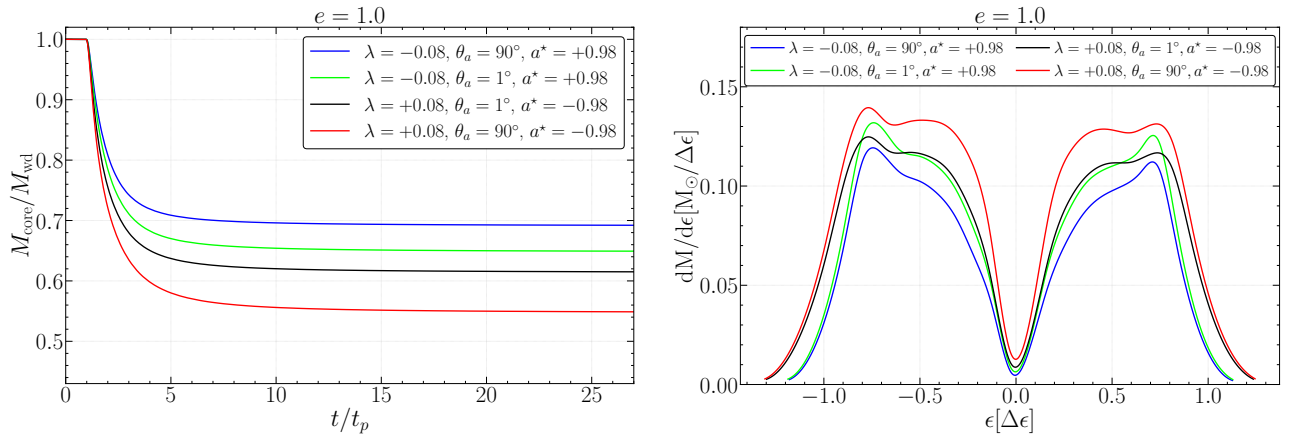


Figure 5. Change in the variations of tidal debris due to WD spin for the specified values of breakup fraction λ , inclination angle θ_a and BH spin a^* . **Left Panel:** The variation of core mass fraction, $M_{\text{core}}/M_{\text{wd}}$ against normalized time. **Right Panel:** The variation of differential mass distribution dM/de with respect to normalized specific energy.

overall inclination effect since the WD spin does not affect the tidal potential exerted by the BH. Among all possible configurations, we find that in the equatorial plane, the case with WD spin $\lambda = +0.08$ and BH spin $a^* = -0.98$ results in the maximum mass disruption, while the case with $\lambda = -0.08$ and BH spin $a^* = +0.98$ results in the minimum mass disruption. The corresponding maximum and minimum mass disruptions in the $\theta_a = 1^\circ$ plane fall between these two extremes; see the left panel of Figure 5. In Table 2, we have displayed all the relative differences⁴ in core mass

⁴ Relative differences are computed with respect to the results corresponding to non-spinning WD.

fraction between spinning and non-spinning WD for the corresponding a^* and θ_a . Based on these results, we calculate the debris differential mass distribution with their specific energies. The distribution profiles are generated from the post-disruption snapshot taken at $t \approx 0.21$ hr after the bound core mass has saturated and before the debris has accreted. In this case, the spread in the $\theta_a = 1^\circ$ and $\theta_a = 90^\circ$ planes is not the same for both BH spins, unlike the non-spinning scenario. This indicates that the spread is primarily influenced by the stellar spin, rather than the spin of the BH. We observe a slightly wider (for $\lambda = +0.08$) or narrower (for $\lambda = -0.08$) spread in the $dM/d\epsilon$ distribution profiles due to the WD spin for the specified configurations, as shown in the right panel of Figure 5. This variation occurs reasonably due to the small change observed in the core mass fraction in the presence of WD spin.

a^*	Relative Difference in $M_{\text{core}}/M_{\text{wd}}$ between $\lambda = 0.00$ and $\lambda = +0.08$		Relative Difference in $M_{\text{core}}/M_{\text{wd}}$ between $\lambda = 0.00$ and $\lambda = -0.08$	
	$\theta_a = 1^\circ$	$\theta_a = 90^\circ$	$\theta_a = 1^\circ$	$\theta_a = 90^\circ$
+0.98	2.99%	2.62%	2.09%	1.84%
-0.98	3.01%	3.70%	2.10%	2.47%

Table 2. Comparison of the relative difference in $M_{\text{core}}/M_{\text{wd}}$ for different λ values, BH spins a^* , and angular orientations θ_a in a parabolic orbit.

3.2. Observables

We now analyze the observable variations with the inclination angle, BH spin, and WD spin as a result of the tidal interaction. TDEs in parabolic trajectory result in approximately half of the debris bound to the BH and the other half unbound from the BH. The bound part due to its negative specific energy falls back onto the BH and contributes to the mass fallback rate. The fallback rates are calculated directly from the simulation without using the well-known “frozen-in” approximation. We excise a $3r_t$ radius around the BH when the tidal tails and the self-gravitating core move away from the BH after the interaction. Once the bound part starts moving towards the BH and crosses the $3r_t$ radius, it accretes by the BH. We noted the mass accreted by the BH with time, and the numerical derivative of the data is used to compute the fallback rates. This methodology is used by the authors: Coughlin & Nixon (2015), Golightly et al. (2019b), Miles et al. (2020) and Garain et al. (2023). This method for calculating fallback rates is consistently applied throughout this work. In our analysis, we focus exclusively on parabolic orbits to demonstrate the methodology. Elliptical orbits involve various complications, such as debris from both tails contributing to fallback rates. Moreover, while this debris is accreted, the self-bound core can approach the pericenter, leading to further disruption. This multiple interaction between the WD and BH will eventually make the computational analysis more challenging.

In the left panel of Figure 6, the fallback rate is shown to have a lower peak value for the motion in the $\theta_a = 90^\circ$ plane compared to the $\theta_a = 1^\circ$ plane for BH spin of $a^* = +0.98$ (and in the absence of spin of the WD). Again, the reverse behavior is observed for a BH spin of $a^* = -0.98$. Overall, the dynamics suggest that the fallback rate is dominated by the retrograde motion ($a^* = -0.98$ & $\theta_a = 90^\circ$), while the prograde motion ($a^* = +0.98$ & $\theta_a = 90^\circ$) results in a lower fallback rate. The fallback rate for the $\theta_a = 1^\circ$ plane consistently falls between those for prograde and retrograde motions. Similar outcomes also seen in the work by Kesden (2012b). By virtue of the conservation of linear momentum during the partial tidal disruption phase, the bound tail imparts a “kick” to the saturated bound core. Consequently, the bound core can gain sufficient energy to eject from the influence of the BH and become a hypervelocity star (Manukian et al. 2014; Gafton et al. 2015), which increases its specific orbital energy and specific angular momentum. This is quantified by the kick velocity, defined as; $v_{\text{kick}} = \sqrt{\epsilon_{\text{core}} - \epsilon_{\text{in}}}$, where ϵ_{core} and ϵ_{in} denote the specific orbital energy of the bound core and the initial WD, respectively. In the right panel of Figure 6, we demonstrate the effect of inclination on the kick velocity imparted to the saturated WD core for the specified values of a^* and θ_a . The relative gain in the velocity of the bound core due to the kick between prograde and retrograde motion is around 20.5% for $\theta_a = 90^\circ$. The bound core corresponding to $\theta_a = 1^\circ$ has an almost identical kick velocity across both BH spins.

In the presence of a spinning WD, we observe similar effects on the mass fallback rate due to stellar spin, as seen in the case of mass disruption. These changes are influenced by the coupling between the WD spin and the orbital angular momentum, as displayed in the left panel of Figure 7. The inclination effect remains the same as before. The

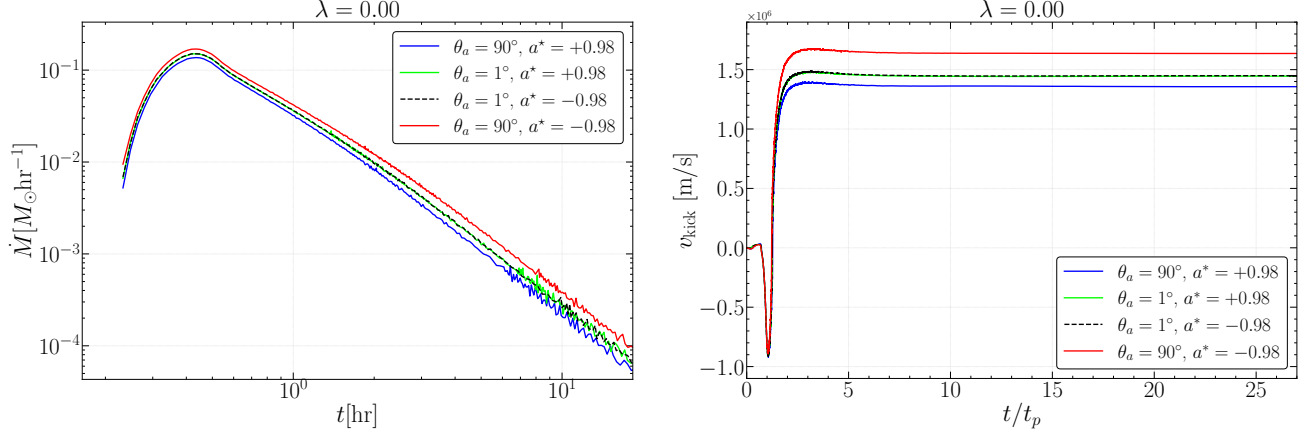


Figure 6. **Left Panel:** Fallback rate plotted against time in hours. **Right Panel:** Kick velocity of bound core plotted against normalized time.

maximum peak fallback rate is observed for the BH spin $a^* = -0.98$ and $\theta_a = 90^\circ$, while the minimum occurs for $a^* = +0.98$ and $\theta_a = 90^\circ$. However, we note that the WD spin, with values $\lambda = +0.08$ and $\lambda = -0.08$, leads to a

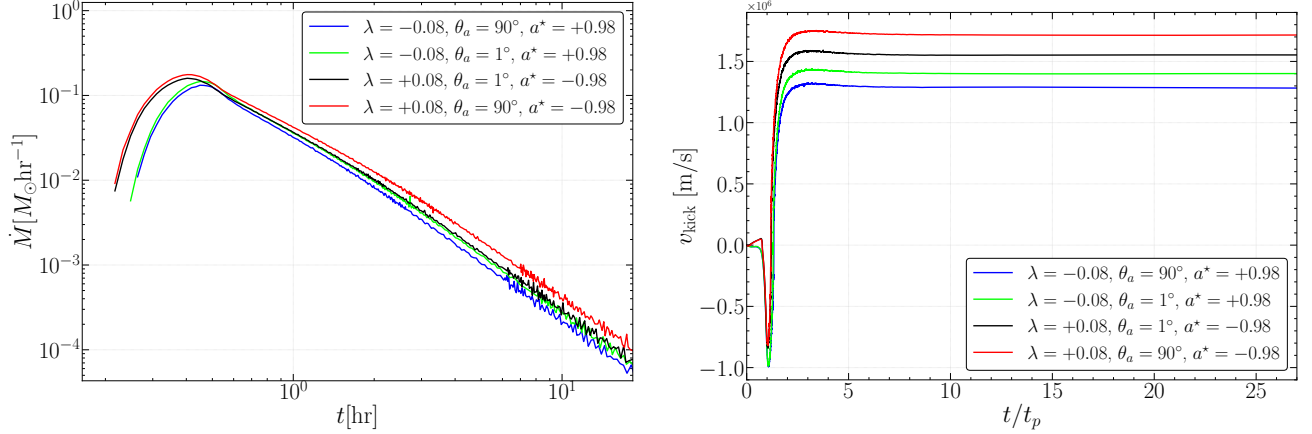


Figure 7. Variation in the presence of WD spin. **Left Panel:** Fallback rate plotted against time in hours. **Right Panel:** Kick velocity of bound core plotted against normalized time.

slight increase and decrease in the peak fallback rate, respectively, for both $\theta_a = 1^\circ$ and $\theta_a = 90^\circ$. This occurs due to the fact that tidal torque finally aligns the stellar spin in the prograde direction with respect to the orbital motion of the WD. In the case of initial retrograde stellar spin, the star is first spun down and then spun up while reaching the pericenter. On the other hand, for an initial prograde stellar spin, the tidal torque enhances the same so that more matter can be stripped off the WD as it reaches the pericenter. This anti-alignment also results in a small difference between the fallback times of the most bound debris onto the BH. In this case, the maximum relative change in the kick velocity for the WD bound core on $\theta_a = 90^\circ$ plane between the given λ and a^* becomes 33.86%, as found in the right panel of Figure 7.

3.3. Gravitational Wave Emission

TDEs are promising sources of gravitational radiation. When a WD passes close to the pericenter of its orbit around a BH, the tidal disruption generates a peak in the GW amplitude. This burst-like behavior occurs because the stellar debris becomes too dispersed after pericenter passage, suppressing strong GW emission beyond r_p . The emission can be characterized by an amplitude h and a duration $t \sim 1/f$, where f is the frequency of the GW.

We computed the GW emission using the quadrupole approximation, following the method outlined in Rossow et al. (2009). The GW polarization amplitudes, $h_+(t)$ and $h_{\times}(t)$, as well as the total amplitude, $|h(t)| =$

$\sqrt{|h_+(t)|^2 + |h_\times(t)|^2}$, were evaluated over time for various tidal disruption scenarios. Our system setup and assumptions follow [Toscani et al. \(2022\)](#), with the pericenter of the WD's orbit along the y -axis and the system observed face-on, which maximizes the GW signal. For inclined orbits, the system was rotated into the x - y plane before calculating the GW emission using the expressions from [Maggiore \(2007\)](#).

Figure 8 illustrates the GW polarization amplitudes h_+ and h_\times , along with the strain magnitude $|h|$ for a parabolic orbit around a BH with spin parameter $a^* = +0.98$, plotted against time (in seconds). The relative amplitude difference $|h|$ between the equatorial and off-equatorial planes is about 0.34%. The strain in the plane with inclination $\theta_a = 1^\circ$ is slightly higher than in the $\theta_a = 90^\circ$ plane, consistent with the findings of [Toscani et al. \(2022\)](#). In our case, the penetration factor β is not large enough to produce a significant change. A slight shift in the peak is also observed, which is attributed to a small variation in the passage time to the pericenter. For the BH spin $a^* = -0.98$, this pattern reverses, with the amplitude in the $\theta_a = 90^\circ$ plane becoming larger. Notably, the relative amplitude difference increases to approximately 0.6%, slightly higher than in the $a^* = +0.98$ case. We also verified that rotation does not introduce significant changes in the GW polarisation amplitude. The GW amplitude was found to be approximately 1.83×10^{-22} , with a corresponding frequency of about 2.4×10^{-2} Hz. At a source-to-observer distance of $d = 20$ Mpc, these values are consistent with our numerical simulations, highlighting the potential for detecting such signals in the context of multi-messenger astronomy.

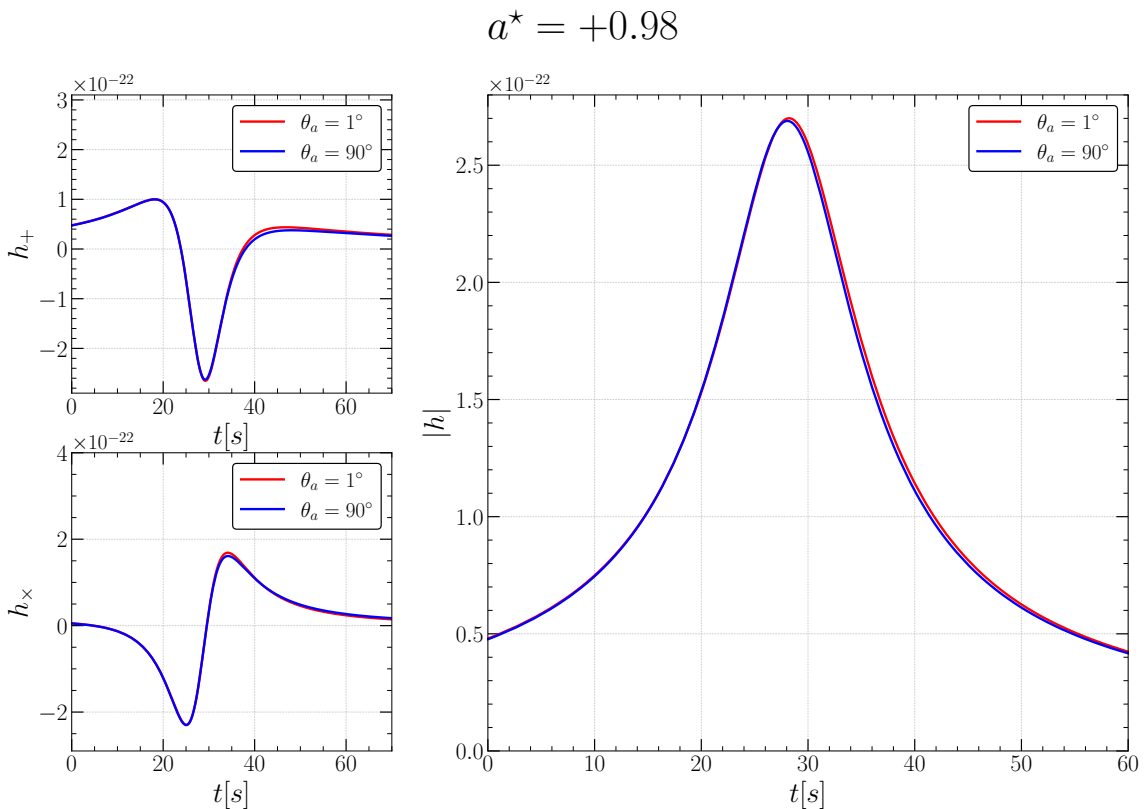


Figure 8. GW polarisation amplitudes by a WD-IMBH system on a parabolic orbit at a distance of $d = 20$ Mpc from us, plotted with respect to the time (in seconds). **Top Left Panel:** h_+ polarization seen face-on **Bottom Left Panel:** h_\times polarization seen face-on **Right Panel:** Root-square-sum amplitude.

4. DISCUSSIONS AND CONCLUSIONS

In this work, we have performed a suite of numerical simulations using smoothed particle hydrodynamics to analyze partial tidal disruption of spinning and non-spinning WDs around Kerr IMBHs in off-equatorial orbits. Our findings emphasize the complex interplay between spin, orbital inclination, and orbital motion in determining the nature of

debris distribution, mass fallback rates, and the ejection of the bound core during TDEs. We quantify the effects of inclination on the tidal disruption observables and compare the observables in the off-equatorial orbits with the equatorial ones. Our main observation here is that as far as WD mass loss, debris mass distribution with specific energy, kick velocity to the self-bound core, and fallback of debris onto the BH are concerned, off-equatorial results lie somewhere in between extreme cases of equatorial ones as depicted in Figures 2, 3 and 4. For example, the peak fallback rate for partial TDEs from equatorial parabolic orbits in IMBHs was analyzed in Garain & Sarkar (2024a). It was shown there that these rates might substantially differ from the quintessential $t^{-9/4}$ scaling known for partial disruption from super massive BHs. Here we find that for off-equatorial orbits, these rates fall within the extremes of the equatorial orbit rates, i.e., from the late time slope of the peak fallback rate depicted in the left panel Figure 7, it is not possible to identify the one corresponding to the $\theta_a = 1^\circ$ orbit, as it might be degenerate with the $\theta_a = 90^\circ$ with a different value of the BH spin. A similar issue is predicted regarding the kick velocity to the self bound core, from the right panel of this figure. We therefore conclude that as far as observations are concerned, TDEs in off-equatorial orbits are degenerate with those in equatorial orbits with different BH spins.

In the context of TDEs involving off-equatorial trajectories, several previous works have reported the explicit dependence of physical observables on BH spin, and orbital inclination, see e.g., Stone & Loeb (2012); van Velzen et al. (2021); Singh and Kesden (2024); Mummery (2024); Stockinger and Shibata (2024). While most previous studies on off-equatorial Kerr orbits involve SMBHs and are performed analytically in Fermi normal coordinates, ours is the first numerical study in the context of IMBHs. To connect these to our results, we show in Figure 9 the tidal stress tensor in units of GM/r_p^3 (with $G = c = 1$) computed in the Fermi normal “tilde” frame that co-rotates with the star, following Marck (1983); Stockinger and Shibata (2024), using the results of Gafton and Rosswog (2019). These are shown here as a function of the non-dimensional quantity r_p/r_s , and tend to their well known Newtonian values (1, 1, -2) in the limit of large r_p . The negative eigenvalue which indicates tidal stretching will be important for us. Recall that as we had mentioned in the introduction, the stress tensors are gradients of the acceleration produced on

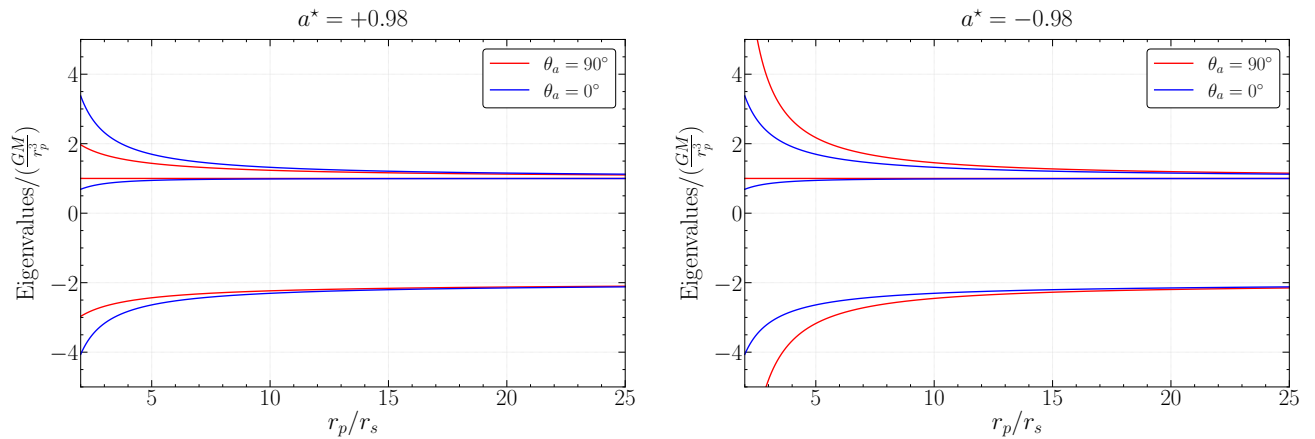


Figure 9. Eigenvalues of the tidal stress tensor in Fermi normal coordinates **Left Panel:** BH spin $a^* = +0.98$. **Right Panel:** BH spin $a^* = -0.98$.

stellar fluid particles. Also, these are independent of stellar mass. From Figure 9, we see that our numerical results in section 3 are at par with those indicated here. Namely, the negative tidal stress is lower for $a^* = +0.98$ compared to $a^* = -0.98$. Also, we find here that the stresses for $\theta_a = 0$ is independent of the BH spin, an effect seen in Figures 2, 3 and 4. In our numerical computations, this “degeneracy” was broken upon introduction of stellar spin – in Fermi normal frame this presumably involves computing the stress tensor in a frame in which the star rotates, but this might be more complicated, see Marck (1983), Stockinger and Shibata (2024).

It is also useful to observe that the eigenvalues of the stress tensor has dimension T^{-2} , so that when normalised by GM/r_p^3 , these are dimensionless and similar for BHs of all masses. Hence, the nature of the graphs in Figure 9 will remain unchanged even for SMBHs. In light of the discussion in the above paragraph, this would indicate that the numerical results presented in this paper should generalise to TDEs involving such BHs as well, but further numerical studies incorporating general relativistic effects in SPH are essential to reach a firm conclusion.

We briefly discuss two other important points here. First, our study is of importance in the context of hypervelocity stars (HVSs), which are stellar objects with velocities exceeding the escape velocity of their host galaxy. Hills (1988). The first observational discovery of an HVS with a radial velocity of 709 km/s in the Galactic rest frame was reported by Brown et al. (2005), with subsequent discoveries of numerous HVSs, as reviewed in Brown et al. (2015). More recently, Koposov et al. (2020) reported the discovery of S5-HVS1, a star with a total velocity of 1755 ± 50 km/s. In our case, the right panels of Figure 6 and Figure 7 indicate similar kick velocities which can potentially result in detectable HVSs. However, whether such a star has been created due to an off-equatorial interaction with an IMBH is difficult to predict. Secondly, we find a small change in the GW signal for off-equatorial orbits as compared to equatorial ones, in Figure 8. In addition to the one reported in the main test, we computed the GW signal with $\beta = 1.8$ and $r_p = 10.02r_g$ with BH spin $a^* = -0.98$, assuming that the Newtonian approximation to the stellar fluid dynamics is still valid. Here we get a relative change of 2.6% between equatorial and off-equatorial orbits in the GW amplitude. Clearly, deeper encounters increase the difference between the GW amplitudes, in lines with what has been reported in Toscani et al. (2022).

ACKNOWLEDGMENTS

We acknowledge the support and resources provided by PARAM Sanganak under the National Supercomputing Mission, Government of India, at the Indian Institute of Technology Kanpur. The work of DG is supported by grant number 09/092(1025)/2019-EMR-I from the Council of Scientific and Industrial Research (CSIR). The work of TS is supported in part by the USV Chair Professor position at IIT Kanpur, India. The work of AM is supported by Prime Minister's Research Fellows by Ministry of Education, Govt. of India.

DATA AVAILABILITY STATEMENT

The data underlying this article will be shared upon reasonable request to the corresponding author.

REFERENCES

- Abbott, R., Abbott, T. D., Abraham, S., et al. 2020, *PhRvL*, 125, 101102.
doi:10.1103/PhysRevLett.125.101102
- Amaro-Seoane, P., Audley, H., Babak, S., et al. 2017, arXiv:1702.00786. doi:10.48550/arXiv.1702.00786
- Balsara, D. S. 1995, *Journal of Computational Physics*, 121, 357. doi:10.1016/S0021-9991(95)90221-X
- Banerjee P., Paul S., Shaikh R., Sakar T., 2019, *Phys. Lett. B* 795, 29. doi:10.1016/j.physletb.2019.05.048
- Banerjee, P., Garain, D., Chowdhury, S., et al. 2023, *MNRAS*, 522, 4332. doi:10.1093/mnras/stad1284
- Brown, W. R., Geller, M. J., Kenyon, S. J., et al. 2005, *ApJL*, 622, L33. doi:10.1086/429378
- Brown, G. C., Levan, A. J., Stanway, E. R., et al. 2015, *MNRAS*, 452, 4297. doi:10.1093/mnras/stv1520
- Cao, Z., Jonker, P. G., Wen, S., et al. 2023, *MNRAS*, 519, 2375. doi:10.1093/mnras/stac3539
- Carter, B. 1968, *Physical Review*, 174, 1559.
doi:10.1103/PhysRev.174.1559
- Chandrasekhar, S. 1935, *MNRAS*, 95, 207.
doi:10.1093/mnras/95.3.207
- Cherepashchuk, A M, 2016, *Phys.-Usp.* 59 702.
doi:10.3367/UFNe.2015.12.037736
- Chilingarian, I. V., Katkov, I. Y., Zolotukhin, I. Y., et al. 2018, *ApJ*, 863, 1. doi:10.3847/1538-4357/aad184
- Coughlin, E. R. & Nixon, C. 2015, *ApJL*, 808, L11.
doi:10.1088/2041-8205/808/1/L11
- Ferrari V., Gualtieri L., Pannarale F., 2009, *Class. Quant. Gravity* 26, 125004. doi:10.1088/0264-9381/26/12/125004
- Gafton, E., Tejada, E., Guillochon, J., et al. 2015, *MNRAS*, 449, 771. doi:10.1093/mnras/stv350
- Gafton, E. & Rosswog, S. 2011, *MNRAS*, 418, 770.
doi:10.1111/j.1365-2966.2011.19528.x
- Gafton, E., and Rosswog, S., 2019, *MNRAS* 487, 4790.
doi:10.1093/mnras/stz1530
- Garain, D., Banerjee, P., Chowdhury, S., et al. 2023, *JCAP*, 2023, 062. doi:10.1088/1475-7516/2023/11/062
- Garain, D. & Sarkar, T. 2024, *ApJ*, 967, 167.
doi:10.3847/1538-4357/ad3dfa
- Garain, D. & Sarkar, T. 2024, arXiv:2401.17031.
doi:10.48550/arXiv.2401.17031
- García-Senz, D., Cabezón, R. M., Blanco-Iglesias, J. M., et al. 2020, *A&A*, 637, A61.
doi:10.1051/0004-6361/201936837
- Golightly, E. C. A., Coughlin, E. R., & Nixon, C. J. 2019, *ApJ*, 872, 163. doi:10.3847/1538-4357/aafd2f
- Golightly, E. C. A., Nixon, C. J., & Coughlin, E. R. 2019, *ApJL*, 882, L26. doi:10.3847/2041-8213/ab380d
- Greene, J. E., Strader, J. and Ho, L. C. 2020, *ARA&A*, 58, 257. doi:10.1146/annurev-astro-032620-021835

- Guillochon, J. & Ramirez-Ruiz, E. 2013, *ApJ*, 767, 25.
doi:10.1088/0004-637X/767/1/25
- Haas R., Shcherbakov R. V., Bode T., Laguna P., 2012, *ApJ*749, 117. doi:10.1088/0004-637X/749/2/117
- Hairer, E., Lubich, C., & Wanner, G. 2003, *Acta Numerica*, 12, 399. doi:10.1017/S0962492902000144
- Harry, G. M., Fritschel, P., Shaddock, D. A., et al. 2006, *Classical and Quantum Gravity*, 23, 4887.
doi:10.1088/0264-9381/23/15/008
- Hayasaki, K., Zhong, S., Li, S., et al. 2018, *ApJ*, 855, 129.
doi:10.3847/1538-4357/aab0a5
- Herant, M. 1994, *Mem. Soc. Astron. Italiana*, 65, 1013
- Hills, J. G. 1975, *Nature*, 254, 295. doi:10.1038/254295a0
- Hills, J. G. 1988, *Nature*, 331, 687. doi:10.1038/331687a0
- Ishii M., Shibata M., Mino Y., 2005, *PhRvD*71, 044017.
doi:10.1103/PhysRevD.71.044017
- Ivanov P. B., Chernyakova M. A., Novikov I. D., 2003, *MNRAS*388, 147. doi:10.1046/j.1365-8711.2003.06028.x
- Jankovic T., and Gomboc A., 2023, *ApJ*946, 25.
doi:10.3847/1538-4357/acb8b0
- Jonker, P. G., Arcavi, I., Phinney, E. S., et al. 2022, *The Tidal Disruption of Stars by Massive Black Holes* (Berlin: Springer)
- Kepler, S. O., Kleinman, S. J., Nitta, A., et al. (2004) *MNRAS*375, 1315.
doi:doi.org/10.1111/j.1365-2966.2006.11388.x
- Kızıltan, B., Baumgardt, H., & Loeb, A. 2017, *Nature*, 542, 203. doi:10.1038/nature21361
- Koposov, S. E., Boubert, D., Li, T. S., et al. 2020, *MNRAS*, 491, 2465. doi:10.1093/mnras/stz3081
- Kormendy J. and Ho L. C. 2013 *ARA&A*, 51 511.
doi:10.1146/annurev-astro-082708-101811
- Kesden, M. 2012, *PhRvD*, 85, 024037.
doi:10.1103/PhysRevD.85.024037
- Kesden M., 2012, *PhRvD*, 86, 064026.
doi:10.1103/PhysRevD.86.064026
- Kilic, M., Kosakowski, A., Moss, A. G., et al. 2021, *ApJL*, 923, L6. doi:10.3847/2041-8213/ac3b60
- Lin, D., Strader, J., Romanowsky, A. J., et al. 2020, *ApJL*, 892, L25. doi:10.3847/2041-8213/ab745b
- Luo, J., Chen, L.-S., Duan, H.-Z., et al. 2016, *Classical and Quantum Gravity*, 33, 035010.
doi:10.1088/0264-9381/33/3/035010
- Maggiore, M. 2007, *Gravitational Waves: Volume 1: Theory and Experiments*, by Michele Maggiore. ISBN: 9780198570745. Oxford University Press, 2007.
doi:10.1093/acprof:oso/9780198570745.001.0001
- Manasse F. K., and Misner C. W., 1963, *J. Math. Phys.* 4, 735. doi:10.1063/1.1724316
- Manukian, H., Guillochon, J., Ramirez-Ruiz, E., et al. 2014, *ApJL*, 782, L13. doi:10.1088/2041-8205/782/1/L13
- Marck J. A., 1983, *Proc. Roy. Soc. Lond. Ser. A*, 385, 431.
doi:10.1098/rspa.1983.0021
- Miles, P. R., Coughlin, E. R., & Nixon, C. J. 2020, *ApJ*, 899, 36. doi:10.3847/1538-4357/ab9c9f
- Mummery, A. 2024, *MNRAS*, 527, 6233.
doi:10.1093/mnras/stad3636
- Price, D. J., Wurster, J., Tricco, T. S., et al. 2018, *PASA*, 35, e031. doi:10.1017/pasa.2018.25
- Rosswog, S., Ramirez-Ruiz, E., & Hix, W. R. 2009, *ApJ*, 695, 404. doi:10.1088/0004-637X/695/1/404
- Sacchi, A. & Lodato, G. 2019, *MNRAS*, 486, 1833.
doi:10.1093/mnras/stz981
- Sato, S., Kawamura, S., Ando, M., et al. 2017, *Journal of Physics Conference Series*, 840, 012010.
doi:10.1088/1742-6596/840/1/012010
- Shibata M., 2003, *ApJ*595, 929. doi:10.1086/377435
- Shapiro, S. L. & Teukolsky, S. A. 1983, *A Wiley-Interscience Publication*, New York: Wiley, 1983.
doi:10.1002/9783527617661
- Singh, T. and Kesden, M., 2024, *PhRvD*109, 043016. doi: 10.1103/PhysRevD.109.043016
- Springel, V. 2005, *MNRAS*, 364, 1105.
doi:10.1111/j.1365-2966.2005.09655.x
- Stockinger, M., and Shibata, M., 2024, *PhRvD*110, 043038.
doi: 10.1103/PhysRevD.110.043038
- Stone, N. & Loeb, A. 2012, *PhRvL*, 108, 061302.
doi:10.1103/PhysRevLett.108.061302
- Stone, N. C., Kesden, M., Cheng, R. M., et al. 2019, *General Relativity and Gravitation*, 51, 30.
doi:10.1007/s10714-019-2510-9
- Takekawa, S., Oka, T., Iwata, Y., et al. 2019, *ApJL*, 871, L1. doi:10.3847/2041-8213/aafb07
- Tejeda, E., Gafton, E., Rosswog, S., et al. 2017, *MNRAS*, 469, 4483. doi:10.1093/mnras/stx1089
- Toscani, M., Lodato, G., Price, D. J., et al. 2022, *MNRAS*, 510, 992. doi:10.1093/mnras/stab3384
- van Velzen, S., Pasham, D. R., Komossa, S., et al. 2021, *SSRv*, 217, 63. doi:10.1007/s11214-021-00835-6
- Volonteri, M. 2012, *Science*, 337, 544.
doi:10.1126/science.1220843
- Wiggins P., and Lai, D., 2000, *ApJ*532, 530.
doi:10.1086/308565
- Yu, Q. & Tremaine, S. 2003, *ApJ*, 599, 1129.
doi:10.1086/379546